Observations of Sea Ice Melt from Operation IceBridge Imagery

Nicholas C. Wright[1], Chris M. Polashenski[1,2], Scott T. McMichael[3], Ross A. Beyer[3,4]

[1]Thayer School of Engineering, Dartmouth College, Hanover, NH, USA
[2]U.S. Army Cold Regions Research and Engineering Laboratories, Hanover, NH, USA
[3]NASA Ames Research Center, Moffet Field, CA, USA
[4]SETI Institute, Mountain View, CA, USA

Corresponding author: Nicholas Wright (ncwright.th@dartmouth.edu)

Abstract. The summer albedo of Arctic sea ice is heavily dependent on the fraction and color of melt ponds that form on the ice surface. This work presents a new dataset of sea ice surface fractions along Operation IceBridge (OIB) flight tracks derived from the Digital Mapping System optical imagery set. This dataset was created by deploying version 2 of the Open Source Sea-ice Processing (OSSP) algorithm to NASA's Advanced Supercomputing Pleiades System. These new surface fraction results are then analyzed to investigate the behavior of meltwater on first-year ice in comparison to multiyear ice. Observations herein show that first-year ice does not ubiquitously have a higher melt pond fraction than multiyear ice under the same forcing conditions, contrary to established knowledge in the sea ice community. We discover and document a larger possible spread of pond fractions on first-year ice leading to both high and low pond coverage, in contrast to the uniform melt evolution that has been previously observed on multiyear ice floes. We also present a selection of optical images that captures both the typical and atypical ice types, as observed from the OIB dataset. We hope to demonstrate the power of this new dataset and to encourage future collaborative efforts to utilize the OIB data to explore the behavior of melt pond formation Arctic sea ice.

1 Introduction

The extent and age of the Arctic sea ice cover has declined since the beginning of the satellite record in 1979 (Stroeve et al., 2012). Ice melt is accelerated through albedo feedback cycles initiated by surface melt decreasing the ice cover's reflectance (Curry et al., 1995; Perovich et al., 2003). Understanding changes in sea ice properties that impact albedo, particularly melt pond coverage, is important to parameterizing sea ice in global climate models (Hunke et al., 2013; Serreze et al., 2009). In-situ observations that could support developing this understanding are sparse, difficult to acquire, and may not be broadly representative (Perovich, 2002a; Wright and Polashenski, 2018). Remote sensing platforms provide a path to understanding sea ice surface change over larger scales. Newly developed computational techniques provide the means to analyze large remotely sensed datasets (Miao et al., 2015; Webster et al., 2015; Wright and Polashenski, 2018). The NASA Operation IceBridge project (OIB) has collected large amounts of high-resolution optical imagery of sea ice with the Digital Mapping System (DMS) (Dominguez, 2010, updated 2017). At ~10cm resolution, these images capture the ice surface in fine detail – but it is challenging to convert them to quantitative measures of ice conditions.

A new technique for analyzing high-resolution optical imagery of sea ice has recently been developed and demonstrated (Wright and Polashenski, 2018). This technique, named the Open Source Sea-ice Processing algorithm (OSSP), automatically analyzes input imagery and classifies image area into four primary surface type categories: 1) snow and unponded ice, 2) dark or thin ice, 3) melt ponds and submerged ice, and 4) open ocean. Categories 1 and 2 are often combined to create a unified ice category. Several improvements and new features that define version 2 of OSSP are presented here. This version was used to create a new dataset by deploying the algorithm on a large scale to process the entirety of the NASA OIB optical image dataset. This dataset is now publicly available for community use and for other studies leveraging the IceBridge data suite. This publication is intended partially to serve as supporting documentation for those uses.

The summer portion of the new dataset is then used to evaluate existing hypotheses about melt pond formation on Arctic sea ice. One such hypothesis describes the prevalence of ponds on first-year sea ice (FYI) versus multiyear ice (MYI). It has been widely stated that FYI has a higher average fractional pond coverage than MYI over the complete melt season (Eicken et al., 2004; Fetterer and Untersteiner, 1998a; Morassutti and Ledrew, 1996; Perovich and Polashenski, 2012). This would contribute to positive ice-albedo feedbacks, since the higher pond fraction would lower albedo of FYI, re-enforcing the transition to a younger ice pack. The reasoning most cited for expecting higher pond coverage on FYI is related to ice and snow topography (Barber and Yackel, 1999; Derksen et al., 1997; Eicken et al., 2004). When ice grows from open Arctic waters, it tends to form in flat, undeformed pans or fairly level pancake fields (Weeks, 2010). Though these pans are subsequently broken and ridged by dynamic forces, in most parts of the Arctic a large fraction of FYI remains level. When surface melt begins on level FYI floes, melt water is unconstrained by topography and spreads to cover a large fraction of the surface. On MYI, however, the ice has survived prior melt seasons that create more complex surface topography even in areas without mechanical deformation. The meltwater is then contained by the prior year's melt-formed topography into well-defined pools. The result *should be* that FYI would tend to experience greater pond coverage than MYI. Indeed, this has been presented by several authors as a likely change in the Arctic (Eicken et al., 2004; Polashenski et al., 2012).

64   It is important to note that pond evolution over the melt season is highly variable and is controlled
65   by the balance of melt water inflow and outflow rates, surface topography, and snow depth. There are
66   four stages that characterize seasonal melt pond formation described in Eicken et al. (2002) and
67   paraphrased as follows: (1) Initial onset of ponds above sea level with a rapid increase in areal coverage,
68   (2) increased outflow allowing drainage to sea level with a decline in areal extent, (3) graduate increase
69   in areal coverage due to ice melting to below ocean freeboard, and (4) refreezing. Despite a common
70   understanding of high pond coverage on FYI, a collection of previous observations (Eicken et al., 2004;
71   Perovich, 2002; Webster et al., 2015) have shown the possibility that FYI has lower pond coverage than
72   MYI under certain circumstances. For example, in stage 2 areal coverage drops significantly more on FYI
73   than it does on MYI (Polashenski et al., 2012). Observations at the SHEBA drifting ice camp found that
74   10-30% of the FYI in the region formed few melt ponds. Measurements there linked this observation to
75   snow cover: Ice with little or no snow cover and with more than 0.5m snow cover had less than 1% pond
76   coverage (Eicken et al., 2004). Webster et al., (2015) found regions where FYI started ponding much
77   later than MYI, though the FYI ultimately developed higher pond coverage later in the summer. A new
78   observational dataset of melt ponds on sea ice from OIB is used here to assess pond coverage
79   differences between ice age at the height of summer melt (July), and to expand previous observations of
80   pond-free FYI to regional scales.

81   A second, related, hypothesis on the behavior of FYI melt ponds suggests two summer melt
82   evolution pathways exist: one which yields high pond fraction, and one that yields near-zero pond
83   fraction (Perovich, 2002a; Polashenski et al., 2017), depending on early season ice permeability and the
84   duration of surface flooding. Our new observations of pond coverage over large areas of FYI provide
85   additional insight. Here, the OSSP-labeled OIB images were used to assess the variation in pond
86   coverage on FYI and the prevalence of pond-free floes within the Chukchi and Beaufort Seas. To
87   accomplish this, a method of post-processing has been developed that determines the size of sea ice
88   areas devoid of pond coverage as a metric to quantitatively address the prevalence of low pond
89   coverage. This new analysis reveals that FYI pond coverage indeed exhibits both pathways, but that
90   there is *not* a strict duality – FYI pond coverage appears to occupy all states across the near-zero to high
91   coverage space. While the OIB image dataset provides large spatial coverage over long flight transects,
92   the lack of temporal coverage makes it impossible to directly link these snapshots of pond coverage to
93   any specific pond evolution process.

94   **2 Methods**

95   **2.1 Data Sources**

96   The datasets described herein are the result of processing NASA Operation IceBridge optical DMS
97   imagery. The DMS images were acquired with a Canon EOS 5D Mark II digital camera which has a 10cm
98   horizontal ground resolution and a spatial footprint of ~600x400m when used at the survey altitude of
99   1500 feet (Dominguez, 2010, updated 2017), and is available for download at the National Snow and Ice
100   Data Center (NSIDC). 87 IceBridge flights were processed, occurring between 2010 and 2018. The OIB
101   flights were categorized into freezing and melting conditions, which map to the spring/fall and summer
102   campaigns respectively. The mean date of melt onset in the Chukchi Sea, Beaufort Sea, and Central
103   Arctic from 1979-2012 was May 17, May 28, and June 10 respectively (Bliss et al., 2014). Spring flights
104   took place before these dates (March to mid-May, typically), and summer flights well after (mid to late

105   July). No flights took place during melt or freeze onset transitional phases, making this a clean
106   categorization: The flights between March and May were categorized as freezing condition flights (no
107   melt ponds expected), and those taken in July were categorized as melting condition flights (melt ponds
108   expected). One flight during fall freeze-up (October 5) was processed and was grouped with the spring
109   set. Using this delineation, there were 9 flights during melting conditions and 78 flights during freezing
110   conditions. Of the 9 melting condition flights, 4 occurred in 2016 originating from Utqiaġvik, Alaska, and
111   4 occurred in 2017 originating from Thule AFB, Greenland. There was an additional summer flight
112   departing from Utqiaġvik on July 20th, 2016, that was not processed due to constant cloud cover
113   obscuring the images.

114   A graphic of the flight tracks for all OIB sea ice flights processed, colored by freezing/melting
115   condition status, is presented in Fig. 1. For the majority of this paper, we will focus on the melting
116   season (summer) flights, colored in yellow. Spring data products are posted for use by the community.
117   We anticipate that future analysis of spring flight data will help confirm lead identification in analysis of
118   altimetry data and provide statistics on lead size and spacing and morphology useful to studies of, for
119   example, blowing snow loss to leads or ice dynamics.

120   **2.2 OSSP Algorithm Improvements**

121   A number of improvements have been made to OSSP since the initial version 1 release described in
122   Wright and Polashenski (2018). These changes can be divided into three categories: 1) Those that alter
123   the algorithms used to classify images, 2) those which add new features, and 3) those which improve
124   code efficiency but do not alter the core methodology. Changes that fall into category (3)
125   reimplemented existing functions for improved performance and decreased computational resource
126   usage. These will not be discussed in detail as they do not change the results.

127   **2.2.1 Algorithm Refinements**

128   OSSP is an object-based segmentation and classification image processing algorithm. In version 1, edge
129   detection for segmentation was done by applying a Sobel-Feldman filter to the image, amplifying the
130   resulting values to highlight strong edges, and thresholding low gradient value pixels to remove weak
131   edges. The amplification factor and threshold value were both presented as tuning parameters that
132   could control the number and strength of edges to detect in the image. In version 2, image edges are
133   instead found with a Canny edge detector (van der Walt et al., 2014), which has three built-in tuning
134   parameters: A gaussian filter with chosen radius that removes noise from the image, a high threshold
135   which selects strong edges, and a low threshold which defines weak edges. These three parameters can
136   be selected based on the quality of the input image and the degree of segmentation sought. The change
137   in edge detection method does not significantly shift the behavior of the OSSP method but allows the
138   user to better tune the segmentation to specific images. The remainder of the OSSP code uses
139   methodology as presented in Wright and Polashenski (2018).

140   **2.2.2 New Features**

141   Four new features were added for processing the OIB optical image dataset: 1) An image quality
142   analyzer which flags excessive cloud cover or haze, 2) an automatic white balance correction function, 3)

143   expanded training datasets specific to OIB images, including shadow detection in spring images, and 4)
144   orthorectification to a flat plane WGS84 spheroid.

145   Clouds and semi-opaque haze are common in OIB imagery. These often partly obscure the surface
146   and prevent accurate image classification. An automated algorithm has been added that detects
147   obscured images so that they can be removed from analysis. The quality check is based on applying a
148   Fourier transformation to the image to detect the ratio of high and low frequency features. It is an
149   implementation of the De and Masilamani (2013) method, where the quality score is the percent of
150   image pixels that have a frequency greater than $1/100,000^{th}$ of the maximum frequency. Poor quality
151   images were empirically found to have a score of less than 0.025, potentially unusable images had a
152   score between 0.025 and 0.035, and images with a score greater than 0.035 were generally acceptable.

153   A large number of OIB images are taken in poor surface lighting conditions. This is often a result of
154   the aircraft flying under cloud cover or high solar zenith angles. Darker than expected and blue-shifted
155   images are observed under these conditions. Unlike the hazy images flagged by the quality check, these
156   can still be accurately classified. An automatic white balance correction function has been added to
157   standardize the hue and exposure of these images and the resulting image classification. We use a
158   single-point white balance algorithm:

159
$$\begin{bmatrix} R_c \\ G_c \\ B_c \end{bmatrix} = \begin{bmatrix} \dfrac{omax}{R_w} & 0 & 0 \\ 0 & \dfrac{omax}{G_w} & 0 \\ 0 & 0 & \dfrac{omax}{B_w} \end{bmatrix} * \begin{bmatrix} R \\ G \\ B \end{bmatrix}$$

160   where
161
$$omax = \max(R_w, G_w, B_w)$$

162   and (R_w, G_w, B_w) is a chosen white reference pixel, (R,G,B) is the original pixel value triplet, and
163   (R_c, G_c, B_c) is the corrected pixel value triplet. The reference point triplet is chosen automatically based
164   on the image histogram of each color band; it is the smallest value that is both larger than the highest
165   intensity peak and has less than 15% of that peak's pixel counts. This method sets the selected reference
166   point to true white (255,255,255). All other pixels in the image are corrected with the same linear
167   scaling which serves to both adjust the image exposure and rebalance the RGB ratios. The white
168   reference pixel is limited to a minimum value of 200 for images with only a single surface. This prevents
169   them from being improperly stretched so that an open water only image will remain black. The effect
170   this color correction has on two poorly illuminated images is shown in Fig. 2.

171   The OIB dataset has a clear binary division between flights where melt ponds are expected (July),
172   and those where they are not (March–May). This characteristic allows for the utilization of two
173   specialized training datasets–one for each season. The summer training dataset is a new, larger, set than
174   was presented along with OSSP v1.0, including additional points to encompass a wider range of possible
175   ice conditions. The spring training dataset includes a ridge shadow surface classification class and does
176   not include a melt pond category. The shadow detection method was not applied to melting condition
177   images as the typical summer solar zenith angle yields fewer shadows. The algorithm allows melt pond
178   and shadow detection to be used together given the correct training data, but this was not utilized for
179   the creation of the dataset described here. Webster et al., (2015) found that ridge shadows make up less

180   than 0.5% of the ice surface in spring, indicating that any errors due to misclassifying them are small.
181   Removal of the melt pond category from spring images prevented occasional spurious detection of melt
182   ponds and improved the quality of results. The training data creation followed the same technique
183   presented in the OSSP version 1.0 documentation (Wright and Polashenski, 2018). The summer dataset
184   was expanded to a total of 1706 training points, and the spring dataset to a total of 865 points. These
185   training datasets can be found along with the OSSP code at (https://github.com/wrightni/ossp).

186   **2.3 Detecting Pond-Free Ice Areas**

187   The labeled image output by the OSSP algorithm was further analyzed to extract metrics about the
188   spatial distribution of water features in summer. A technique was developed to find contiguous regions
189   of pond-free ice. These regions were defined as a circle with diameter greater than 12m that does not
190   overlap any water feature. First, the labeled image was converted into a binary image separating the
191   snow and ice features from water (i.e. melt ponds plus ocean). Next, the distance from every snow/ice
192   pixel to the nearest water feature was calculated, and peaks with a local maximum distance above a
193   threshold of 12 meters were recorded. Pond free areas are the circle centered at these peaks with a
194   radius of the distance to the nearest water feature. Any two overlapping regions were combined by
195   adding the non-overlapping area of the smaller region to that of the larger region. These pond free
196   regions are divided into two categories, small and large, based on a threshold of a 25 m radius. The
197   thresholds of 12m and 25m were selected to be approximately 2x and 4x the mean caliper diameter of
198   melt ponds (Huang et al., 2016). The number of pond free areas per image was multiplied by the ice
199   fraction (sum of all non-ocean categories) of that image to account for differing ice concentrations
200   between images. Figure 3 shows an example of this detection, where the location of both the small and
201   large regions are marked with small dots and the large regions have a translucent circle showing the size
202   of that region.

203   **2.4 Error**

204   There are several sources of error in OSSP ice type classifications when applied to the DMS dataset.
205   The established accuracy of the OSSP method, on a high-quality input image, is 96% (Wright and
206   Polashenski, 2018). The principle source of error novel to this OIB dataset was due to lower quality
207   images, typically from haze obscuring the surface or poor surface illumination. While automated
208   methods standardize the quality of the input and flag bad images (Section 2.2.2), some input errors
209   remain. The impact of uncorrected haze is twofold: First, it causes the algorithm to misclassify open
210   water as melt pond, and second, it obscures surface type boundaries and causes insufficient image
211   segmentation. Both issues can be understood by looking at how haze changes an optical image: It adds
212   noise to the image, tends to brighten the pixel values, and blurs surface features. As the defining feature
213   of open water is its uniform darkness, a layer of haze makes this surface more like a dark melt pond. The
214   blurring impacts the edge detection algorithm used by OSSP and therefore causes a breakdown of the
215   proper delineation of image surfaces. For the analyses of the summer dataset presented herein, images
216   were manually sifted to remove those scenes that were not flagged by the QA analysis, but were still of
217   questionable quality. Due to the heterogenous nature of sea ice, there is a trade-off between accuracy
218   on a specific image and accuracy on the entire dataset – some images flagged as low quality may be
219   usable with a training dataset tailored to those specific images. Users of this dataset should inspect their
220   region of interest to ensure the image quality meets their desired standard.

3 Results

3.1 Melt pond fraction along OIB flight tracks

In this paper we focus on presenting results from summer images only. Images from 87 IceBridge flights were processed with the OSSP algorithm representing over 900,000 individual images using the methods described above – these results are available for other investigations at the NSIDC archive. Figure 4 maps the track of every melt season OIB flight and plots melt pond fraction observed along these tracks. Melt pond fraction was calculated as the number of melt pond pixels divided by the total ice area (ice pixels + pond pixels). Images where more than 70% of the area was classified as open water are colored black in Figure 4 but were processed normally. Images that were automatically removed due to a low quality score (section 2.2.2) are colored orange, and images that were manually removed due to low image quality are colored red. In total, 40,672 summer images were analyzed, of which 14,876 (36.6%) were flagged with a low quality score, 5,671 (13.9%) were manually removed, and 20,125 (49.5%) were kept for this analysis. The July 20th, 2016 flight was not processed because only about 2% (30 total) of the images were haze free. Note both high variation in pond coverage along track and general regional changes between flights. Some additional variation between flights is due to temporal change, for example it appears a summer snow occurred just prior to the July 19, 2016 flight, lowering the observed pond fraction.

Figure 5 plots 300km of the along-track melt pond fraction for the July 24th, 2017 flight. This figure illustrates the large variability possible in melt pond fraction along track seen in the first half of the flight (top), with a minimum observed fraction of 10% and spikes to greater than 50%. The second half of this flight (bottom) has a more uniform melt pond fraction of ~20%. Four peaks are highlighted in orange where a large blue pond formed on the MYI (See Fig. 11d). Figure 6a zooms in to a 10km subset of this transect, and the surface corresponding to the orange highlighted section is shown in Fig. 6b. The optical image is the result of stitching 23 DMS images together. The highlighted peak in melt pond fraction occurs on a section of FYI between two multiyear floes. This case follows the prevailing hypothesis about the differences between pond formation on MYI and FYI. The relatively flat FYI section allows melt ponds to spread over the surface more evenly, resulting in a higher melt pond coverage, despite encountering the same atmospheric conditions as the MYI on either side. It is also possible that melt water from the MYI drains to the lower elevation FYI (Fetterer and Untersteiner, 1998a).

3.2 Influence of Ice Type on Melt Pond Fractions

Each summer transect was categorized into first-year ice, multiyear ice, or mixed ice based on manual inspection of those flight's images. The delineation of ice type was based on pond shape, color, and distribution as well as ice surface topography (Johnston and Timco, 2008). The flights classed as a single ice type had at least 90% (estimated from visual inspection) of that type. Melt pond statistics for single ice type flights are shown as box and whisker plots in Fig. 7, where each flight is colored by its ice type categorization; blue for FYI and green for MYI. In these plots the box outline shows the 75th and 25th percentile, the middle line displays the median, the whiskers show 1.5x the interquartile range, and the red points are outliers. Generally, the 2016 flights departing from Utqiaġvik, Alaska, observed FYI while the 2017 flights departing from Thule AFB, Greenland, observed MYI. There are three exceptions to this categorization: July 13, 2016 and July 19, 2016 contain both ice types, where small pockets of MYI were included in the northern sections of an otherwise primarily FYI region, and flight A on July 25th, 2017

262 covers FYI. Statistics for the two mixed ice type flights are plotted separately in Fig. 8, where each flight
263 is divided into FY or MY ice categories.

264   Figure 7 reveals two insights into the difference in melt pond fractions between FYI and MYI. First,
265 there is no obvious difference in the median pond fraction between flights, and second, there is more
266 variance in the pond fractions on FYI. The variance is described by the interquartile range, the mean of
267 which is 0.1 for the first-year flights and 0.05 for the multiyear flights. In other words, while FYI exhibited
268 a wider range of possible pond fractions, the average coverage is not observed to be higher than on
269 MYI. The difference in timing and region between OIB flights precludes drawing general conclusions
270 about differences in median melt pond fraction between ice types. However, two flights that contained
271 both FY and MY ice were selected for further analysis to investigate melt pond statistics across ice that
272 experienced similar forcing conditions: July 19, 2016 and July 13, 2016. The portions of these transects
273 that depict each ice type were manually determined. Results, delineated by ice type, for these two
274 flights are shown in Fig. 8. The key observation here is that the two flights show opposite relationships:
275 On July 19 the FYI has a lower median pond fraction, while on July 14, the FYI has a higher median pond
276 fraction. Previous work has shown the possibility for FYI to have lower pond cover than MYI at local
277 scales (i.e. individual floes) (Eicken et al., 2004, Webster et al., 2015). Our results support this
278 observation and show that it can also happen at regional scales. That pond coverage is more variable on
279 FYI than it is on MYI suggests that while ponds evolve differently on each type there is not a simple
280 relationship in mean pond fraction. In other words, one cannot conclude that FYI has either higher or
281 lower pond fractions than MYI.

3.3 Observations of Pond-Free First-year Ice

283 The frequency at which FYI develops low pond coverage was investigated using the pond-free region
284 detection algorithm to find large unponded areas. Figure 9 shows the results of applying this algorithm
285 to selected segments of the July 19, 2016 flight. Panel (a) shows the results for a portion of primarily FYI
286 with high pond coverage, (b) shows a region of FYI that has many areas of pond-free ice, and (c) shows
287 results from a section of MYI. The ice analyzed for Fig. 9a is what we understand would be considered as
288 a common state for FYI in an advanced state of melt, where ponds have drained to sea level but a high
289 portion of the ice floe remains below freeboard and yields a uniformly high pond fraction. This state
290 coincides with the third stage of pond evolution. This contrasts with the FYI analyzed for Fig. 9b where,
291 while melt ponds are still present, there are large open areas of pond free ice. The ponds on the MY floe
292 are regularly distributed and the fractional pond coverage shows little variance. This could coincide with
293 stage 2 of pond evolution, where ponds have drained and none remain above freeboard, or to a region
294 where ponds never formed. A timeseries would be required to distinguish these paths. Expanding from
295 these regions of this specific flight, 17% of all summer FYI images processed for this study have 3 or
296 more large pond free regions. This reinforces previous observations by Eicken et al. (2004) that
297 estimated 10 to 30% of FYI surrounding the SHEBA ice camp had "low or zero pond cover". In contrast,
298 in the MYI portion of this dataset, only 5% of images have 3 or more large pond free regions. While
299 there is a clear difference between the MYI and FYI types, the important observation here is the large
300 percentage of FYI that has lower than expected pond coverage.

3.4 Snapshots of a Summary Sea Ice Cover

In processing the Operation IceBridge optical imagery dataset, we have had the unique opportunity to review a significant library of images detailing different sea ice states, looking at thousands of square km of sea ice. So few people actually observe the sea ice that notions of what is 'typical' or unusual are still not well known. In Figures 10 and 11 we present some examples of what we have observed to be 'representative' ice states, and examples of ice conditions that are uncommon. The OSSP analyzed results for each frame in Figure 10 and 11 are in Supplement S1 and S2, respectively. These are intended to serve as a qualitative summary of the extensive OIB observations, against which future campaigns can be quickly compared. For each presented image we label the noted features based on the frequency at which we have observed them. Along an arbitrary 100km transect of ice in a given melt state; *common* describes a feature that can be expected on more than half of the ice, *occasional* describes features that would be expected to show up 5-10 times, and *infrequent* describes a feature that may present once or twice.

Sea ice scenes shown in Fig. 10: **(a)** FYI that shows a wide range of the possible melt pond fractions, ranging from pond free to high pond coverage; *occasional*. **(b)** Highly ponded level FYI scene in early melt, where ice appear as islands in a sea of water. Such ice was *common* in large areas in the Chukchi sea. **(c)** FYI with high pond fraction and very interconnected pond structure. *Common*; this represents the generally understood behavior of FYI. Here we also see that ponds preferentially form towards the middle of the floe leaving a pond-free border around the edge. The floe-edge gradients are particularly strong in this image, the pond-free border is an *occasional* feature. **(d)** Example of a floe where ponds preferentially form away from the edges. These small floes with central ponds were common in broken FYI. **(e)** Shorefast level ice in the Lincoln Sea. Ponds have started to drain already, as evidenced by the drainage channels visible throughout the ice. This type of relatively low coverage and consolidated ponds were *infrequent* in the OIB dataset, but may be common of ice in this region. We speculate that deep snow dunes and thick ice are responsible. **(f)** This image shows a region that appears to have had a recent summer snowfall event. The snow serves to fill shallow ponds with slush or to completely cover them and significantly lowers pond fraction – *infrequent* in the OIB dataset as it is dependent on specific weather conditions. **(g)** A *common* example of high pond fraction FYI. **(h)** Flat and thin ice pans that are almost completely covered by melt water, this scene is *common* for late stages of melt on FYI.

Sea ice scenes shown in Fig. 11: **(a-c)** *Common* examples of ponded MYI floes with characteristically blue ponds that are well consolidated by surface topography, showing the range of pond fractions that are possible. **(d)** Example of large reservoir-like ponds that were only observed on MYI. These are *occasional* features on large sections of MYI. **(e)** MYI with FYI inclusions from ocean that refroze during the last winter, this is *common* for MYI at lower latitudes, and *occasional* at higher latitudes. In cases of small FYI inclusions in MYI fields like this, the FYI ice is typically darker had has a higher pond coverage. **(f)** An example of low pond coverage MYI – this was *infrequent* in the OIB dataset. **(g+h)** Ponded FYI undergoing drainage, where evidence of previous ponds is still visible. The overall image represents *common* features, but the drainage pattern here is *infrequently* observed, likely due to its short lifespan.

4 Discussion

A common hypothesis in the sea ice community states that FYI has, on average, higher melt pond coverage than MYI. While there is considerable nuance to this statement due to the variability of pond coverage over the temporal domain, it represents a testable hypothesis which our results above did not support. It should be noted that our dataset represents single snapshots in time, and while many melt states were observed, it is impossible to assess complete seasonal averages of melt pond coverage here. There are many factors contributing to areal melt pond coverage differences between FYI and MYI. In the early season, when meltwater sits on impermeable ice above sea level, limited topography causes a similar volume of meltwater to flood larger areas of FYI than it would on rougher MYI. This is supported by observations in early melt stages, which show FYI melt pond coverage in excess of 60%. Such coverage exceeds that seen on MYI at any time (Landy et al., 2014; Polashenski et al., 2012). However, in Stage 2, MPF on FYI tends decline faster than on MYI because the meltwater can drain to sea level at a faster rate (Polashenski et al., 2012). In the late season, after ponds have drained to sea level, it has been argued that thinner FYI will have less buoyancy and less ice area above freeboard than MYI. In contrast, on thicker FYI the level surface would have fewer depressions and more buoyancy, and therefore more ice area above freeboard (e.g. Figure 10d). The relative pond fraction between FYI and MYI depends on the time along the melt evolution and the ice physical properties. Over many melt states observed in the complete summer dataset (Figures 7 and 8), we did not find a statistically significant difference in average pond fraction between FYI and MYI.

An alternate hypothesis about the behavior of FYI ponds emerging in some recent papers is that FYI pond coverage is extremely variable and may have bimodal evolution driven by snow topography and permeability (Perovich, 2002b; Polashenski et al., 2017; Popović et al., 2018). FYI ponds may not form at all under certain circumstances if the ice is highly permeable or lacks snow cover (Polashenski et al., (2017) and references therein). Other observations show very high melt pond coverage that persists even after ponds drain to sea level (Polashenski et al., 2015). This divergence of pond behavior raise the possibility of bimodal behavior wherein some FYI would flood extensively and experience more ponding than MYI while other FYI might not pond at all. The image dataset analyzed in this study does *not* support the bimodal hypothesis, but rather supports the idea that FYI pond coverage is much more variable than MYI, and existing in all states from low to high pond cover. Several factors could be the cause of the high variability seen in our dataset. For example, diurnal effects can play a large role in the melt pond fraction on FYI by significantly changing surface melt rates on short time scales (Eicken et al., 2004; Hanesiak et al., 1999). Alternatively, if ice and snow topography controls pond fraction after ponds drain (Polashenski et al., 2012), FYI where snow dunes or differential melt create surface roughness will have higher pond fraction while ice that is level will be pond-free. As the sea ice topography is highly variable, we would expect corresponding variability in the pond fraction.

Examining the pond coverage in more detail provides evidence that the range of possible melt states is larger on FYI than it is on MYI. In other words, FYI exhibits all possible states between low and high coverage, while MYI pond fraction typically exists within a small window. Returning to the boxplots in Fig. 7, note the larger interquartile range (IQR) of the first-year flights versus the multiyear flights. If we were to accept the traditional hypothesis that all FYI had high pond cover, we would expect the FYI to have a higher median but a similar IQR. However, this is not the case. These observations suggest pond cover on FYI is highly variable, and only in a subset of circumstances does the ice exhibit the expected

381 higher pond fraction. Examples of each behavior are included in Fig. 8. The traditional understanding of
382 melt pond evolution on FYI, where flat undeformed ice allows melt water to spread horizontally and
383 create large areas of pond covered ice is often observed on landfast ice or ice attached to a multiyear
384 floe (e.g. Barber and Yackel, 1999; Derksen et al., 1997; Fetterer and Untersteiner, 1998b; Uttal et al.,
385 2002). For example, Fig. 6b shows a refrozen lead between two MYI floes, where the pond fraction is
386 significantly higher on the flat FYI than on either of the adjoining MYI floes. Along the July 19, 2016
387 transect many of the smaller (less than 200m diameter) freely floating floes of flat FYI exhibited little to
388 no pond cover late in the melt season (as seen in Fig. 10d). We also note many examples of floes that
389 are pond free along their edges, such as in Fig. 10c, and floes that exhibit nearly complete pond
390 coverage (such as 10b,g,h). This dataset, therefore, helps establish that no simple relationship between
391 FYI and MYI ponding exists, and presents the possibility that the transition to FYI is not causing uniformly
392 higher melt pond fraction, as has been expected. Due to the temporal variability in pond evolution,
393 complete timeseries datasets are needed to fully analyze the relationship between MPF and ice age.
394 Understanding the distribution of MPF on basin wide scales would be key to understanding whether the
395 transition from MY to FYI has a net increase on pond prevalence. No large scale, comprehensive
396 observations have been available to resolve the prevalence of such behaviors.

397 **5 Conclusion**

398 A new dataset quantifying sea ice surface fractions observed in Operation IceBridge DMS imagery has
399 been created using the recently developed OSSP algorithm. This dataset classifies the surface coverage
400 into four categories. During the melt season these categories are: 1) snow or thick ice, 2) dark or thin
401 ice, 3) melt ponds and submerged ice, and 4) open water. In freezing conditions, the categories become
402 1) snow or thick ice, 2) dark or thin ice, 3) open water, and 4) ridge shadows. The dataset allows for the
403 investigation of sea ice surface type distributions along OIB transects and opens the door for new
404 studies, both by analysing this dataset in isolation (as demonstrated here), and by combining it with
405 coincident OIB datasets such as ice thickness or ice roughness. This dataset is available at the NSDIC for
406 community use. Future improvements to this dataset should include work towards a more sophisticated
407 haze removal algorithm to apply to the OIB optical images. This will increase accuracy and increase the
408 fraction of images that can be successfully processed.

409 We have investigated snapshots of melt pond coverage differences between FYI and MYI in the
410 Beaufort/Chukchi Sea region for 2016 and the Lincoln Sea for 2017. Our results support previous
411 findings that FYI can have lower pond fraction than MYI under similar forcing conditions. While the
412 results presented herein cannot definitively confirm or refute the hypothesis that FYI has higher mean
413 pond fraction than MYI, the high variability in FYI pond fraction over large regions suggests that the
414 general rule of thumb that FYI should have higher ponding than MYI is too simplistic. Furthermore, the
415 finding that FYI exhibits much larger variance over its temporal evolution indicates that there is not one
416 path that defines the typical pond coverage changes. We did not find sufficient evidence that there is a
417 strict duality in FYI pond evolution either, and we suggest future process studies investigate the
418 mechanisms that drive FYI towards high or low pond fraction and specifically note that time-series
419 image observations and/or field studies may be necessary to unravel this question. The different
420 trajectories that pond development can apparently take on FYI may have large impacts on sea ice
421 modelling efforts, through albedo feedbacks. Furthermore, we suggest combining this new melt pond

422   dataset with data available from the IceBridge Airborne Topographical Mapper to determine the
423   relationship between sea ice topography and melt pond formation.

424

425   *Data and Code Availability.* The OSSP algorithm code is available on github
426   (https://github.com/wrightni/ossp) and the release for this manuscript is archived at zenodo (DOI:
427   10.5281/zenodo.3551033). The pond free detection algorithm is archived at zenodo (DOI:
428   10.5281/zenodo.3971014) and is available at github (https://github.com/wrightni/pondfree_detection).
429   Raw Operation IceBridge DMS imagery is available from the National Snow and Ice Data Center
430   (https://doi.org/10.5067/OZ6VNOPMPRJ0). OSSP generated results are also archived at the NSDIC
431   (https://doi.org/10.5067/1LI57H56EB7G).

432

433   *Author Contributions.* NW was responsible for writing the original draft, creating the data visualizations,
434   review and editing of the manuscript, designing and testing the OSSP software, conceptualization and
435   programming of the pond-free detection algorithm, and formal analysis of the OSSP generated results.
436   CP was responsible for initiating the study, contributing to writing and editing the manuscript, and
437   contributing to methodology and result analysis. SM was responsible for implementing the OSSP
438   software on NASA's Pleiades system, monitoring data processing, and data archiving. RB was responsible
439   for funding acquisition and supervision for the Ames Research Center team and for review and editing of
440   the manuscript draft.

441

442   *Conflicts of Interest.* The authors declare that they have no conflicts of interest.

443

444   *Acknowledgements*. The authors would like to thank NASA's AIST Program whose funding enabled this
445   research. The image processing for this work was carried out on NASA's Advanced Supercomputing
446   Pleiades system.

447   **References**

448   Barber, D. G. and Yackel, J.: The physical, radiative and microwave scattering characteristics of melt
449   ponds on Arctic landfast sea ice, Int. J. Remote Sens., 20(10), 2069–2090,
450   doi:10.1080/014311699212353, 1999.

451   Curry, J. A., Schramm, J. L. and Ebert, E. E.: Sea ice-albedo climate feedback mechanism, J. Clim., 8(2),
452   240–247, doi:10.1175/1520-0442(1995)008<0240:SIACFM>2.0.CO;2, 1995.

453   De, K. and Masilamani, V.: Image Sharpness Measure for Blurred Images in Frequency Domain, Procedia
454   Eng., 64, 149–158, doi:10.1016/J.PROENG.2013.09.086, 2013.

455   Derksen, C., Piwowar, J. and LeDrew, E.: Sea-Ice Melt-Pond Fraction as Determined from Low Level
456   Aerial Photographs, Arct. Alp. Res., 29(3), 345–351, doi:10.1080/00040851.1997.12003254, 1997.

457   Dominguez, R.: IceBridge DMS L0 Raw Imagery, Version 1, , doi:10.5067/UMFN22VHGGMH, 2010.

458   Eicken, H., Grenfell, T. C., Perovich, D. K., Richter-Menge, J. A. and Frey, K.: Hydraulic controls of summer
459   Arctic pack ice albedo, J. Geophys. Res. C Ocean., 109(8), doi:10.1029/2003JC001989, 2004a.

460   Eicken, H., Grenfell, T. C., Perovich, D. K., Richter-Menge, J. A. and Frey, K.: Hydraulic controls of summer
461   Arctic pack ice albedo, J. Geophys. Res. Ocean., 109(C8), n/a-n/a, doi:10.1029/2003JC001989, 2004b.

462   Fetterer, F. and Untersteiner, N.: Observations of melt ponds on Arctic sea ice, J. Geophys. Res. Ocean.,
463   103(C11), 24821–24835, doi:10.1029/98JC02034, 1998a.

464   Fetterer, F. and Untersteiner, N.: Observations of melt ponds on Arctic sea ice, J. Geophys. Res. Ocean.,
465   103(C11), 24821–24835, doi:10.1029/98JC02034, 1998b.

466   Hanesiak, J. M., Barber, D. G. and Flato, G. M.: Role of diurnal processes in the seasonal evolution of sea
467   ice and its snow cover, J. Geophys. Res. Ocean., 104(C6), 13593–13603, doi:10.1029/1999JC900054,
468   1999.

469   Huang, W., Lu, P., Lei, R., Xie, H. and Li, Z.: Melt pond distribution and geometry in high Arctic sea ice
470   derived from aerial investigations, Ann. Glaciol., 57(73), 105–118, doi:10.1017/aog.2016.30, 2016.

471   Hunke, E. C., Hebert, D. A. and Lecomte, O.: Level-ice melt ponds in the Los Alamos sea ice model, CICE,
472   Ocean Model., 71, 26–42, doi:10.1016/j.ocemod.2012.11.008, 2013.

473   Johnston, M. E. and Timco, G. W.: Guide for understanding and identifying old ice in summer, in
474   International Conference and Exhibition on Performance of Ships and Structures in Ice 2008, ICETECH
475   2008, pp. 351–358. [online] Available from: http://iabp.apl.wahsington.edu. (Accessed 31 July 2020),
476   2008.

477   Landy, J., Ehn, J., Shields, M. and Barber, D.: Surface and melt pond evolution on landfast first-year sea
478   ice in the Canadian Arctic Archipelago, J. Geophys. Res. Ocean., 119(5), 3054–3075,
479   doi:10.1002/2013JC009617, 2014.

480   Miao, X., Xie, H., Ackley, S., Perovich, D. and Ke, C.: Object-based detection of Arctic sea ice and melt
481   ponds using high spatial resolution aerial photographs, Cold Reg. Sci. Technol., 119, 211–222,
482   doi:10.1016/j.coldregions.2015.06.014, 2015.

483   Morassutti, M. P. and Ledrew, B. F.: Albedo and depth of melt ponds on sea-ice, Int. J. Climatol., 16(7),
484   817–838, doi:10.1002/(SICI)1097-0088(199607)16:7<817::AID-JOC44>3.0.CO;2-5, 1996.

485 Perovich, D. and Polashenski, C.: Albedo evolution of seasonal Arctic sea ice, Geophys. Res. Lett., 39(8),
486 n/a-n/a, doi:10.1029/2012GL051432, 2012.

487 Perovich, D., Grenfell, T., Richter-Menge, J., Light, B., Tucker, W. and Eicken, H.: Thin and thinner: Sea ice
488 mass balance measurements during SHEBA, J. Geophys. Res. Ocean., 108(C3),
489 doi:10.1029/2001JC001079@10.1002/(ISSN)2169-9291.SHEBA1, 2003.

490 Perovich, D. K.: Aerial observations of the evolution of ice surface conditions during summer, J. Geophys.
491 Res., 107(C10), 8048, doi:10.1029/2000JC000449, 2002a.

492 Perovich, D. K.: Aerial observations of the evolution of ice surface conditions during summer, J. Geophys.
493 Res., 107(C10), 8048, doi:10.1029/2000JC000449, 2002b.

494 Polashenski, C., Perovich, D. and Courville, Z.: The mechanisms of sea ice melt pond formation and
495 evolution, J. Geophys. Res. Ocean., 117(C1), n/a-n/a, doi:10.1029/2011JC007231, 2012.

496 Polashenski, C., Perovich, D. K., Frey, K. E., Cooper, L. W., Logvinova, C. I., Dadic, R., Light, B., Kelly, H. P.,
497 Trusel, L. D. and Webster, M.: Physical and morphological properties of sea ice in the Chukchi and
498 Beaufort Seas during the 2010 and 2011 NASA ICESCAPE missions, Deep Sea Res. Part II Top. Stud.
499 Oceanogr., 118, 7–17, doi:10.1016/J.DSR2.2015.04.006, 2015.

500 Polashenski, C., Golden, K., Perovich, D., Skyllingstad, E., Arnsten, A., Stwertka, C. and Wright, N.:
501 Percolation blockage: A process that enables melt pond formation on first year Arctic sea ice, J.
502 Geophys. Res. Ocean., 122(1), 413–440, doi:10.1002/2016JC011994, 2017.

503 Popović, P., Cael, B. B., Silber, M. and Abbot, D. S.: Simple Rules Govern the Patterns of Arctic Sea Ice
504 Melt Ponds, Phys. Rev. Lett., 120(14), 148701, doi:10.1103/PhysRevLett.120.148701, 2018.

505 Serreze, M. C., Barrett, A. P., Stroeve, J. C., Kindig, D. N. and Holland, M. M.: The emergence of surface-
506 based Arctic amplification, Cryosphere, 3(1), 11–19, doi:10.5194/tc-3-11-2009, 2009.

507 Stroeve, J. C., Serreze, M. C., Holland, M. M., Kay, J. E., Malanik, J. and Barrett, A. P.: The Arctic's rapidly
508 shrinking sea ice cover: a research synthesis, Clim. Change, 110, 1005–1027, doi:10.1007/s10584-011-
509 0101-1, 2012.

510 Uttal, T., Curry, J. A., Mcphee, M. G., Perovich, D. K., Moritz, R. E., Maslanik, J. A., Guest, P. S., Stern, H.
511 L., Moore, J. A., Turenne, R., Heiberg, A., Serreze, M. C., Wylie, D. P., Persson, O. G., Paulson, C. A., Halle,
512 C., Morison, J. H., Wheeler, P. A., Makshtas, A., Welch, H., Shupe, M. D., Intrieri, J. M., Stamnes, K.,
513 Lindsey, R. W., Pinkel, R., Pegau, W. S., Stanton, T. P., Grenfeld, T. C., Uttal, T., Curry, J. A., Mcphee, M.
514 G., Perovich, D. K., Moritz, R. E., Maslanik, J. A., Guest, P. S., Stern, H. L., Moore, J. A., Turenne, R.,
515 Heiberg, A., Serreze, M. C., Wylie, D. P., Persson, O. G., Paulson, C. A., Halle, C., Morison, J. H., Wheeler,
516 P. A., Makshtas, A., Welch, H., Shupe, M. D., Intrieri, J. M., Stamnes, K., Lindsey, R. W., Pinkel, R., Pegau,
517 W. S., Stanton, T. P. and Grenfeld, T. C.: Surface Heat Budget of the Arctic Ocean, Bull. Am. Meteorol.
518 Soc., 83(2), 255–275, doi:10.1175/1520-0477(2002)083<0255:SHBOTA>2.3.CO;2, 2002.

519 van der Walt, S., Schönberger, J. L., Nunez-Iglesias, J., Boulogne, F., Warner, J. D., Yager, N., Gouillart, E.
520 and Yu, T.: scikit-image: image processing in Python, PeerJ, 2, e453, doi:10.7717/peerj.453, 2014.

521 Webster, M. A., Rigor, I. G., Perovich, D. K., Richter-menge, J. A., Polashenski, C. M. and Light, B.:
522 Seasonal evolution of melt ponds on Arctic sea ice, J. Geophys. Res. Ocean., 120(9), 1–15,
523 doi:10.1002/2015JC011030, 2015.

524 Weeks, W.: On Sea Ice, University of Alaska Press. [online] Available from:

525   https://books.google.de/books?id=9S55O6WzuL8C (Accessed 18 January 2018), 2010.

526   Wright, N. and Polashenski, C.: Open-source algorithm for detecting sea ice surface features in high-
527   resolution optical imagery, Cryosphere, 12(4), 1307–1329, doi:10.5194/tc-12-1307-2018, 2018.

528

529

530 **Figures**

531
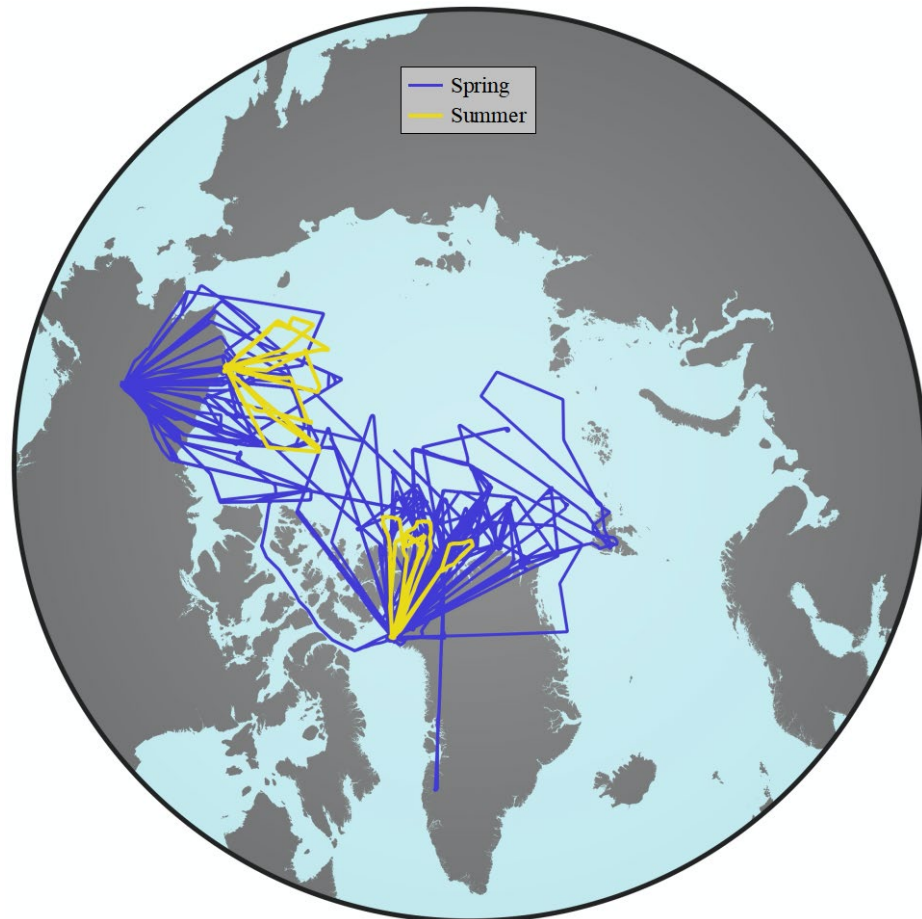
532

533 Figure 1. Plot of all flights processed with OSSP, colored by the melt conditions during the flight. Spring freezing conditions in
534 blue, and summer melting conditions in yellow.

535

536
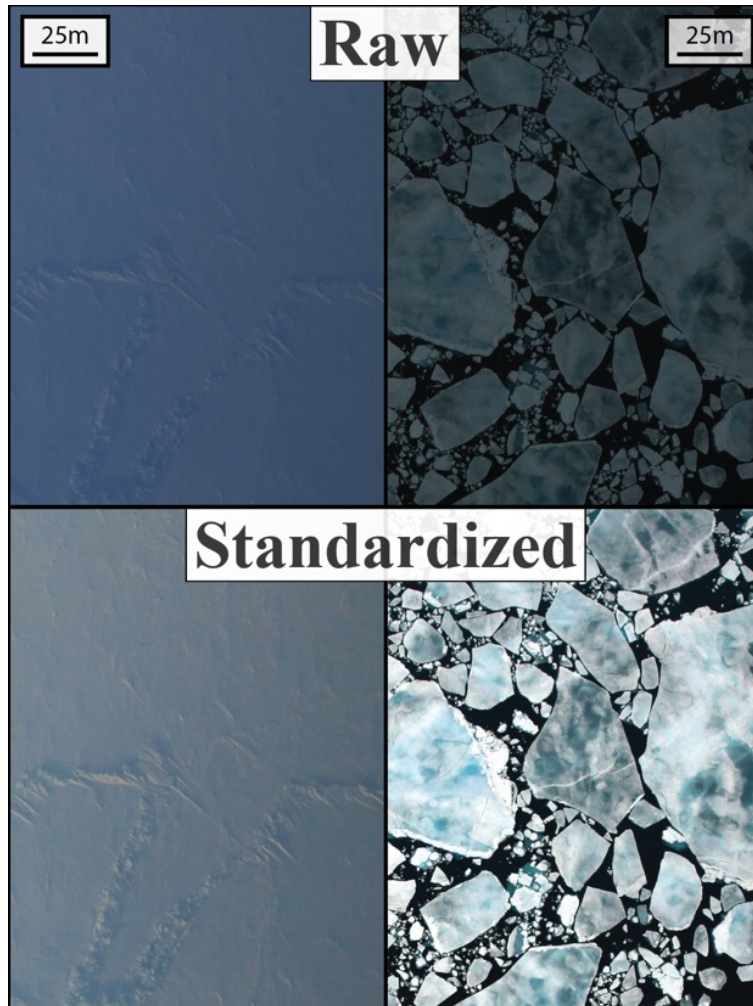
Figure 2. Demonstration of the image preprocessing steps. The raw images (top) have poor surface illumination and a blue hue, both of which have been removed in the standardized images (bottom).

539

540
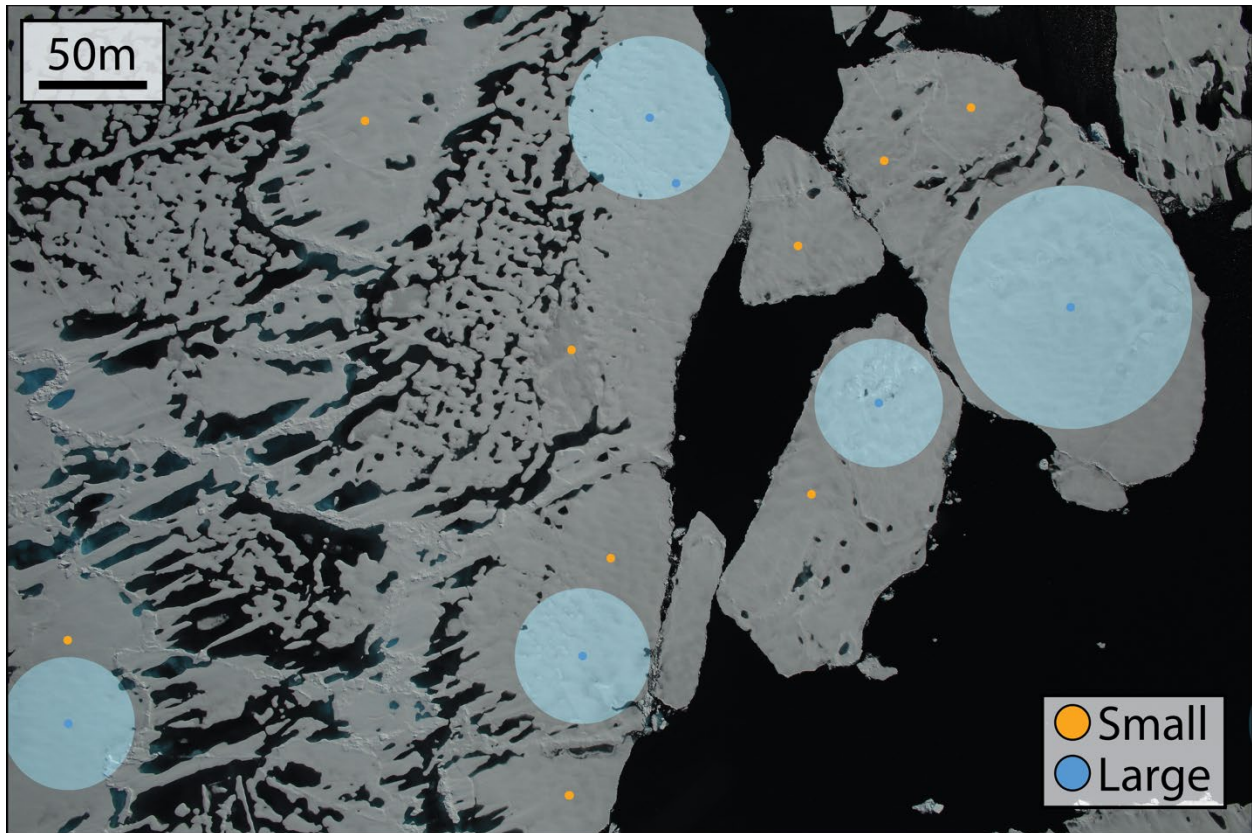
Figure 3. Example of the pond free region detection. Pond free regions are marked by small colored dots, where blue dots indicate the larger regions and orange indicates the smaller ones. Translucent blue circles are drawn with a radius equal to the size of the detected large regions. Blue dots without a translucent circle were merged with a neighboring region.

544
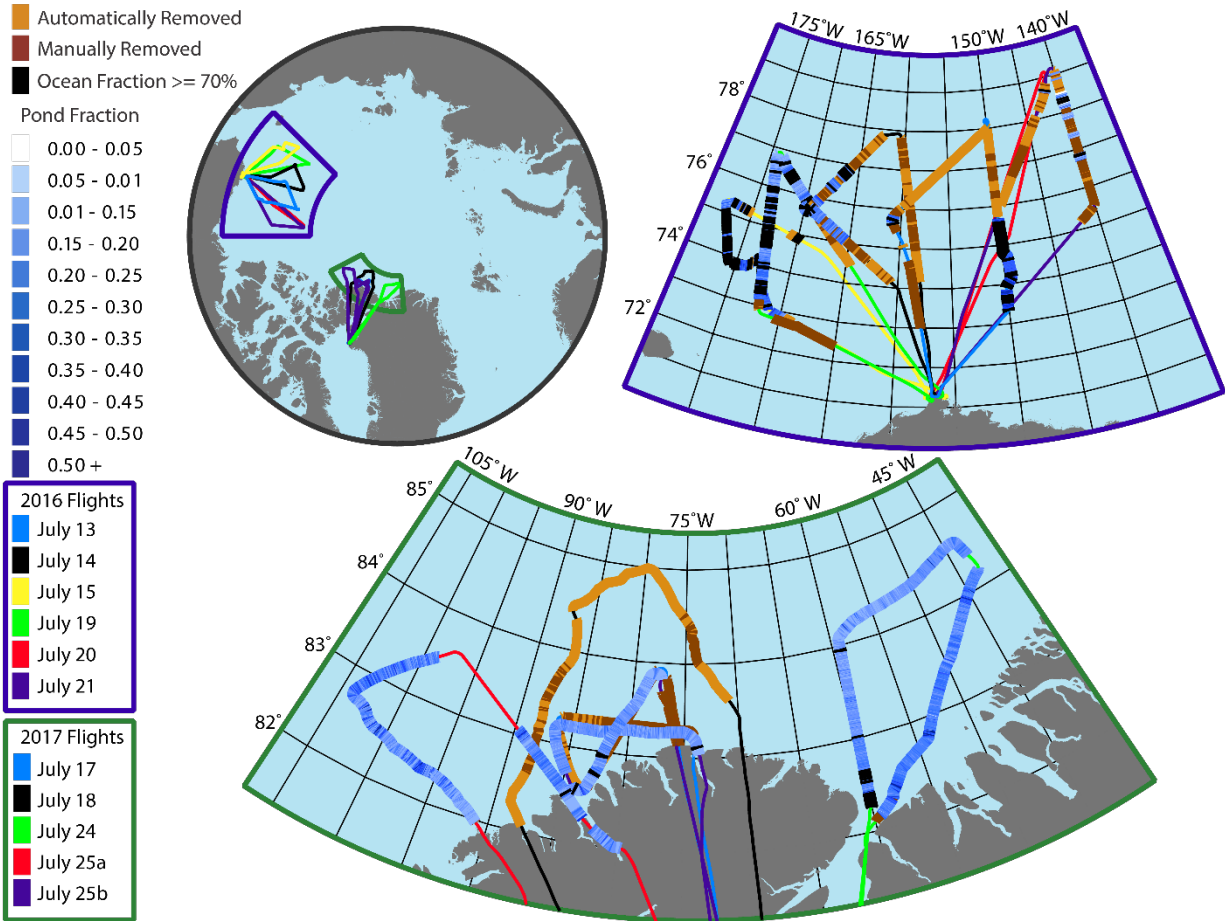
545

546 **Figure 4. Melt pond fraction along OIB summer transects. Automatically and manually removed images are indicated by**
547 **orange and red, respectively. 2016 flights were more prone to haze obscuring the ice surface and therefore have more**
548 **deleted images.**

549

550
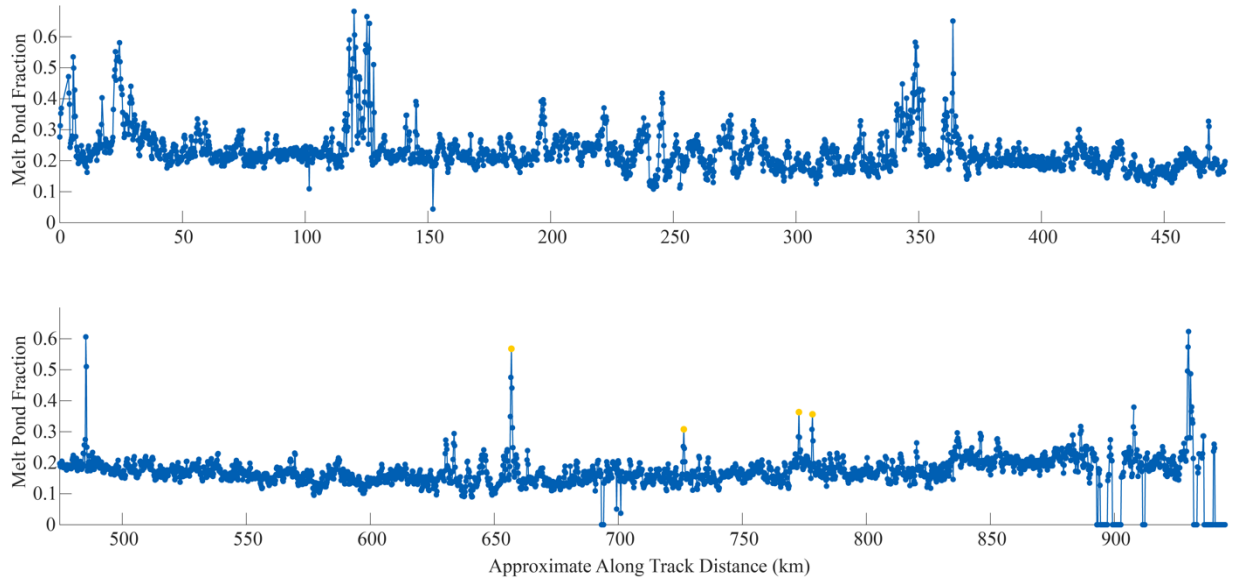
Figure 5. Melt pond fraction along track for flight July 24, 2017. The four orange highlighted points represent areas where there was a large blue pond on the multiyear ice that occupied a large fraction of the image. See Fig. 11d for an example of this feature.

554

555

556

557
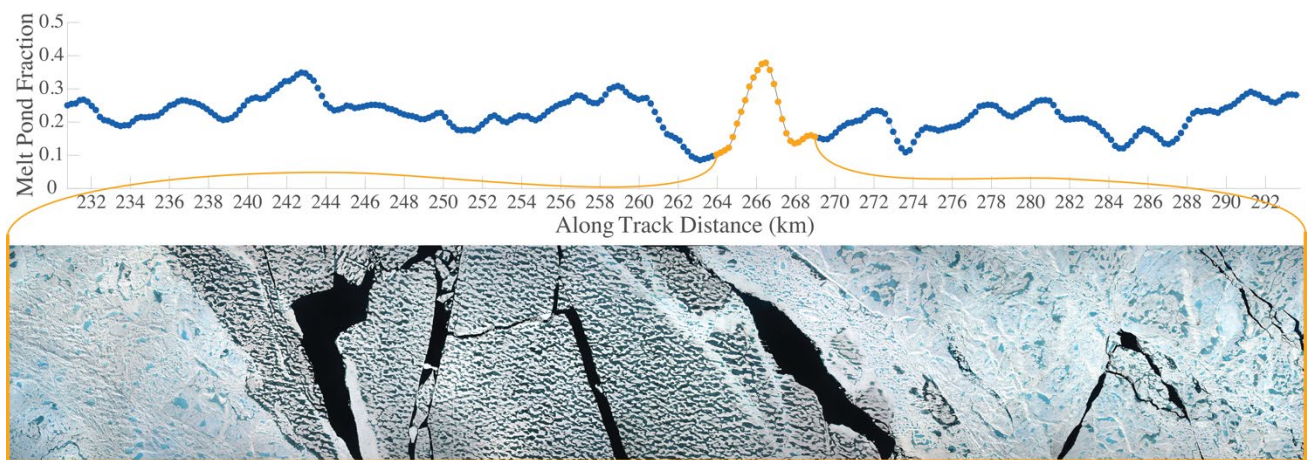
Figure 6. Melt pond fraction along a several kilometer section of the July 24, 2017 flight. The orange highlighted region is depicted as a series of stitched together DMS images that show a first-year inclusion between two multiyear floes.

560

561
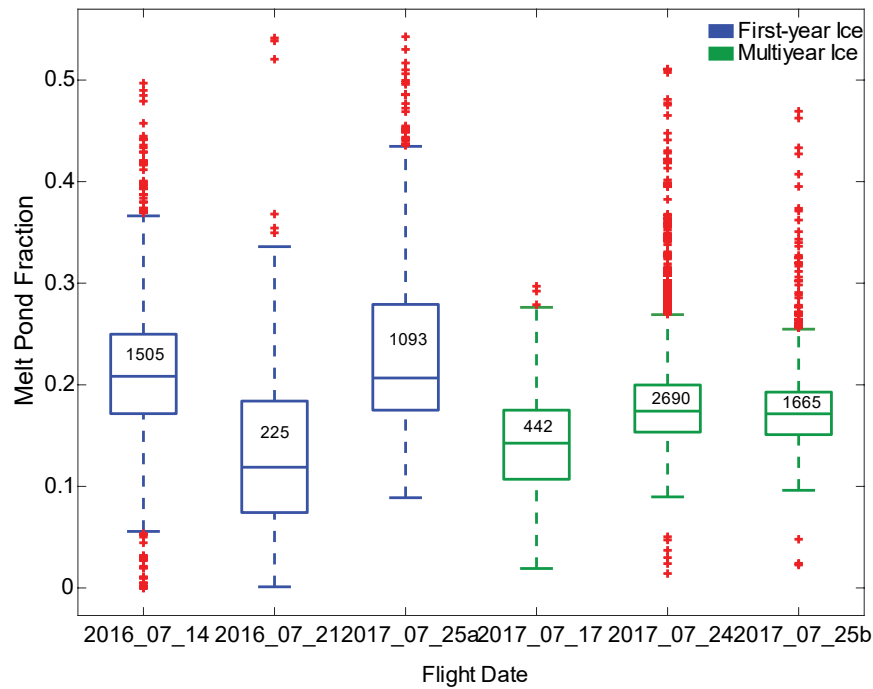
Figure 7. Melt pond statistics from summer OIB flight which contained only a single ice type. Blue corresponds to first-year ice statistics, green to multiyear ice statistics, and red crosses indicate outliers. The number of image frames used to calculate statistics for each flight is included inside the box. The approximate area of each image frame is 0.25 km2

565
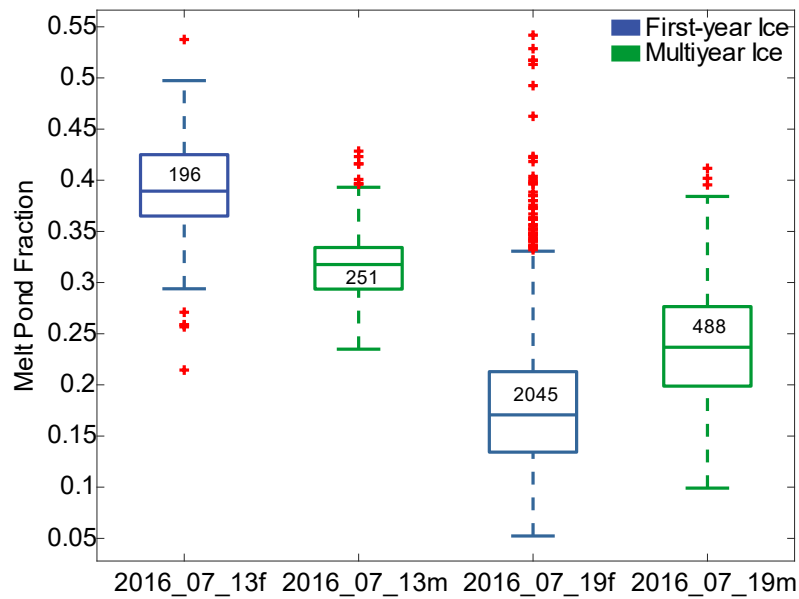
Figure 8. Melt pond statistics from two flights that contain both first-year and multiyear ice. In the July 13 case, multiyear ice has a lower pond fraction, while in the July 19 case the first-year ice has a lower pond fr action. Blue corresponds to first-year ice statistics, green to multiyear ice statistics, and red crosses indicate outliers. The number of image frames used to calculate statistics for each flight is included inside the box. The approximate area of each image frame is 0.25 km²

570

571

572
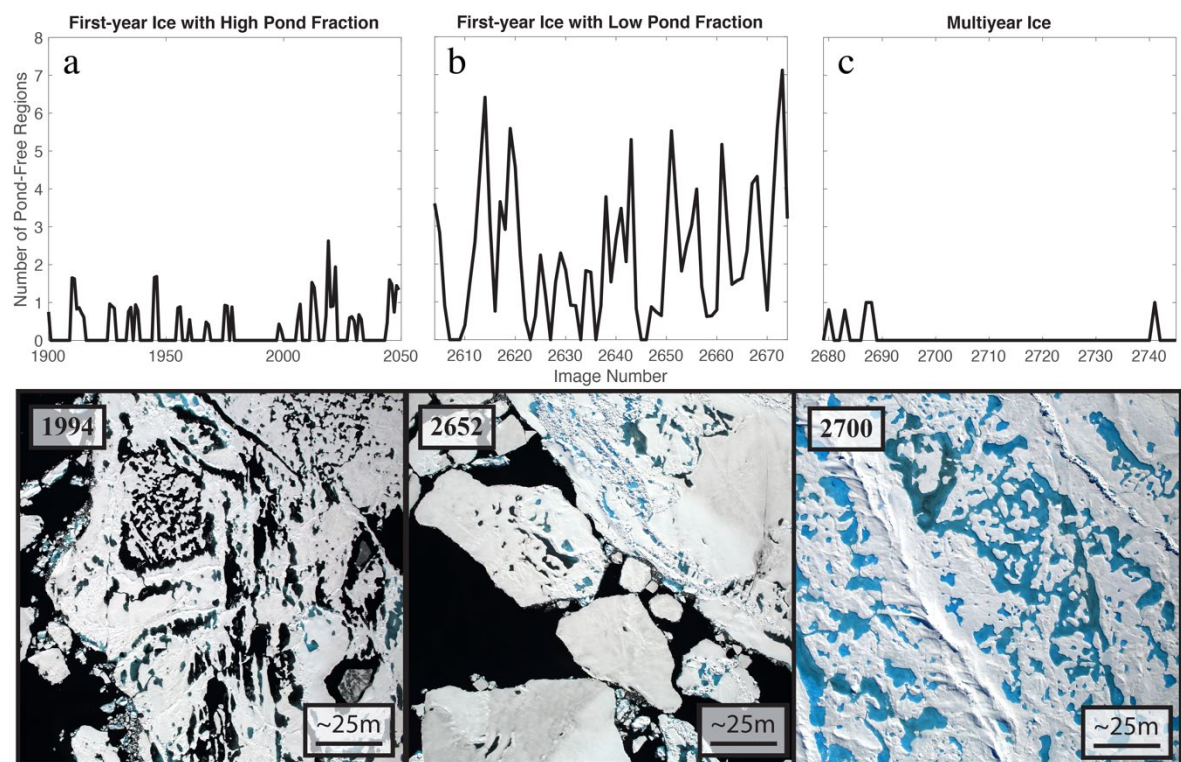
Figure 9. Number of pond-free regions on several regions of sea ice observed during the July 19, 2016 flight (top) and a sample image representing that region of ice (bottom).

575

576
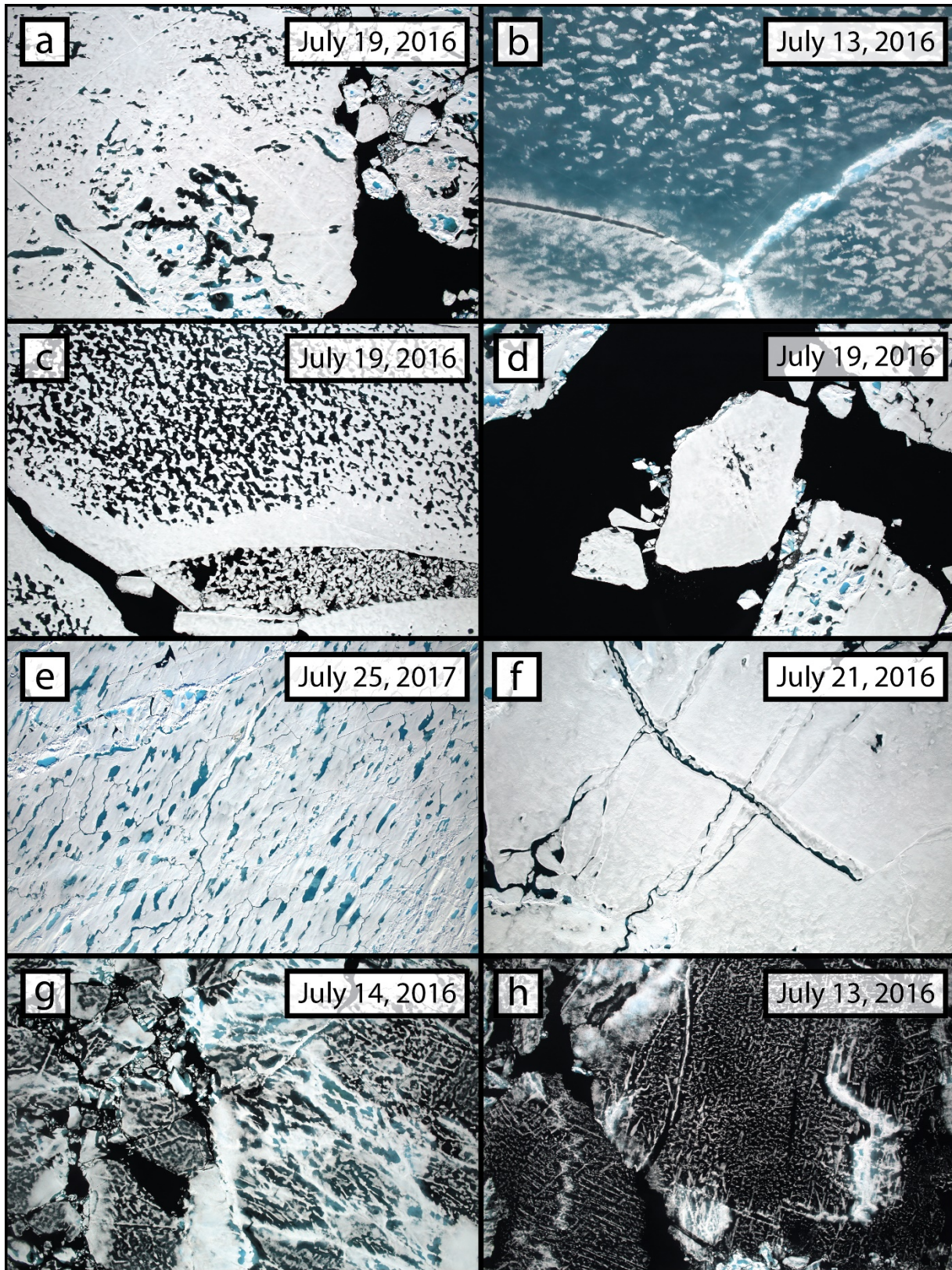
Figure 10. Exhibits of sea ice surface features as seen in the DMS dataset. Each panel is a full IceBridge image, and while flight
altitude affects image resolution, each scene is approximately 600 m by 400 m. See text for full description of each frame.
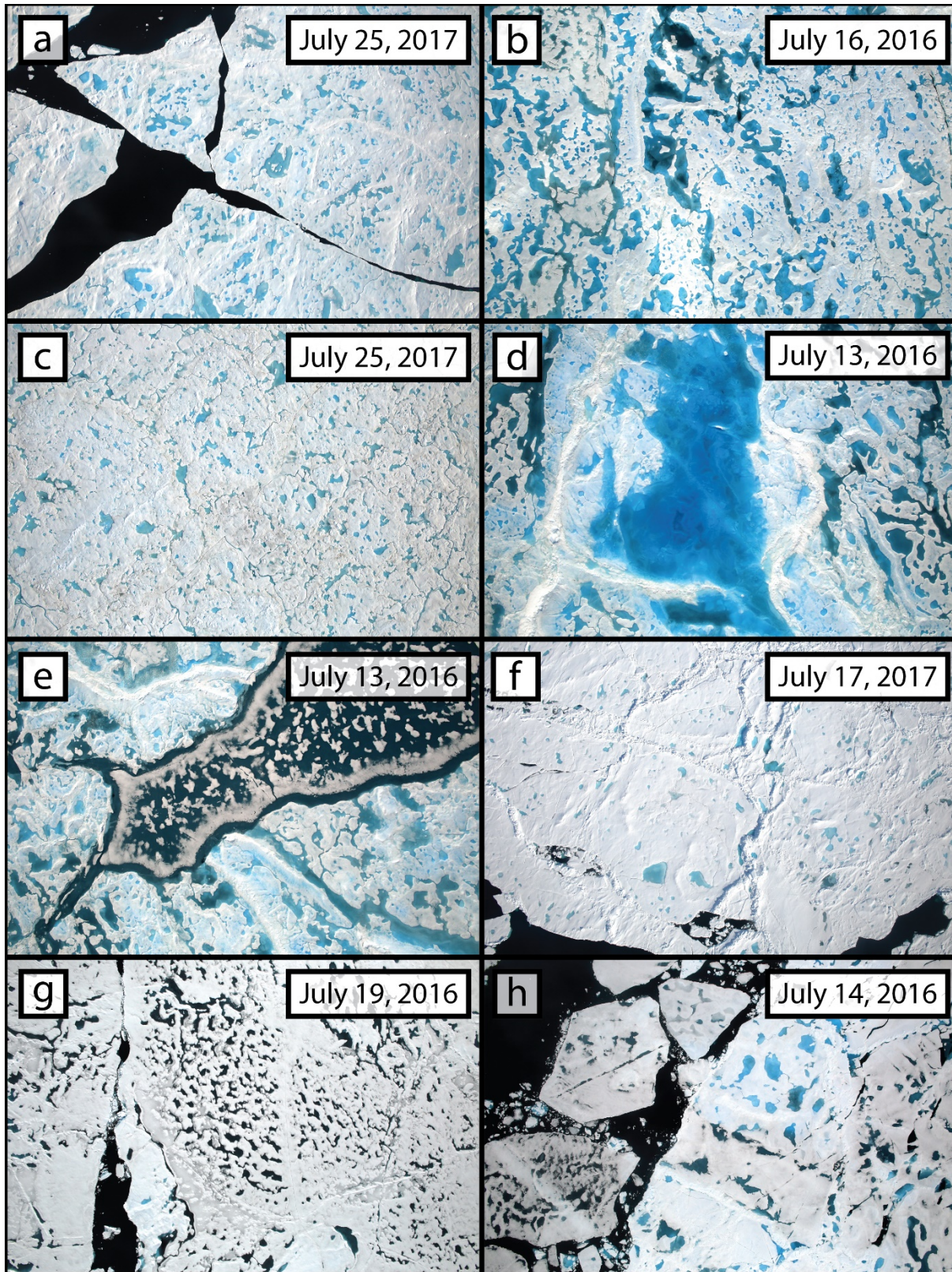
579

580 **Figure 11. Exhibits of sea ice surface features as seen in the DMS dataset. Each panel is a full IceBridge image, and while flight**
581 **altitude affects image resolution, each scene is approximately 600 m by 400 m. See text for full description of each frame.**